Analyst

ROYAL SOCIETY OF CHEMISTRY

PAPER

View Article Online
View Journal | View Issue

Check for updates

Cite this: *Analyst*, 2025, **150**, 3602

An experimental investigation into the focusing behaviours of flagellated and elongated cells in inertial microfluidic devices†

Jessie Howell, *[a,b] Nicole Hall,[b] Sulochana Omwenga,[c] Tansy C. Hammarton [c] and Melanie Jimenez[b]

Received 4th October 2024,
Accepted 30th June 2025

DOI: 10.1039/d4an01288g

rsc.li/analyst

Inertial microfluidics has demonstrated tremendous potential to impact biological – and notably medical – fields, by offering a highly versatile, portable and cost-effective approach to cell focusing and sorting. While the range of applications of inertial devices spans medical diagnostics, bioprocessing or water engineering to mention a few, translation is still impeded by the lack of clear understanding of cell interactions in such devices. This often leads to bespoke designs that take years of development and characterisation for one targeted application, and limited tools for informed optimisation. A more fundamental knowledge of inertial behaviours is key to future translational works and impact, by enabling a deeper understanding of inertial forces in biological systems. Towards this goal, this paper focuses on high-throughput morphological phenotyping of the single-celled, flagellated parasite *Leishmania mexicana* to better understand how variations in cell body length, width and flagellated status impact the focusing patterns of highly non-spherical cells in curved inertial devices. Some of the key findings in this study include (i) flagella do not always alter focusing if body shape is conserved, (ii) the impact of cell shape is specific to a channel design and slight changes in *e.g.*, cell confinement can drastically change focusing patterns, (iii) elongated prolate-like cells align differently depending on their lateral position within a curved channel, and (iv) despite variabilities observed in focusing patterns for elongated *versus* rounder cell phenotypes, large morphological variations can be completely overcome at high Reynolds numbers so that all phenotypes tightly focus at a single and stable position (here, towards the channel outer wall). This last finding, in particular, may open new avenues for highly efficient cell enrichment processes.

Introduction

Inertial microfluidics is an attractive method for sorting particles, offering a high-throughput, label-free and passive method of separation. While sorting cells based on their morphological and mechanical phenotypes has been commonly described, particle size – and more specifically their equivalent diameter – remains the most widely considered factor for driving inertial microfluidic separation and related empirical correlations.[1–3] Biological cells with a round morphological phenotype are often hypothesised to experience inertial forces in a similar fashion to size-matched rigid spherical (*e.g.*, polystyrene) beads, which are consequently used as model systems for design development.[4] Deformability has also been shown to strongly affect focusing behaviours, where the presence of a deformability-induced lift force causes the migration of deformable objects away from more rigid particles.[5–7] This sorting parameter has been successfully applied to *e.g.*, the separation of deformable cancer cells from blood, diagnosis of malaria through identification of infected red blood cells (RBCs) or the purification of manufactured RBCs.[7–9] In contrast, the contribution of shape is less well documented.

Initial work on non-spherical particles in straight inertial microfluidic (IM) channels (*i.e.* without the presence of Dean forces) has reported complex rotational behaviours, with prolate (elongated ellipsoid) particles and oblate (disc-like ellipsoid) particles showing rotations described as "kayaking", "log-rolling" and "tumbling" depending on their position in the flow and the strength of the inertial forces. When these particles focus within the flow, they tend to exhibit a stable rotation with prolate particles "tumbling" and oblate particles "log-rolling".[10–12] By increasing the Reynolds number (Re) further, particles have been shown to align with the flow and

---

[a] Institute of Sensors, Signals and Systems, Heriot-Watt University, Edinburgh, UK
[b] Biomedical Engineering Department, University of Strathclyde, Glasgow, UK. E-mail: jessie.howell@strath.ac.uk
[c] School of Infection and Immunity, University of Glasgow, Glasgow, UK

† Electronic supplementary information (ESI) available. See DOI: https://doi.org/10.1039/d4an01288g

rotate periodically or stop rotating altogether, although this behaviour has not been observed in all studies.[11,13] The longest dimension of a particle (rotational diameter) has been reported as a measurement equivalent to the diameter of a spherical particle, with non-spherical and spherical particles showing a high correlation independent of their shape.[10,14,15] Importantly, however, this pattern does not translate to all non-spherical shapes, *e.g.*, for non-symmetrical particles.[16] It can also be noted that most studies to date have investigated the role of shape in straight IM channels, with fewer systematic explorations in curved designs. Although the relevance of the equivalent diameter has also been shown experimentally for non-spherical objects in Dean flows, divergence in focusing behaviours for differently shaped (but volume- and dimension-matched) beads highlights a higher complexity in fluid-particle interactions compared to straight IM devices.[15] These differences have been partially linked to particle rotation but also to the generation of secondary vortices which can push non-spherical objects away from traditional focusing positions (*e.g.*, away from the inner wall in standard spiral designs).[17] These shape-dependent variations in focusing patterns have been already explored for translation. For example, small and round *Caenorhabditis elegans* eggs were isolated from later development stages with a vermiform shape using a spiral IM channel with a trapezoidal cross section.[18] Keinan showed that sorting of budding yeast in serpentine channels could be used to identify different populations based on cell age.[19] Yeast has also been separated based on shape into different cell cycle stages, obtaining up to 94% purity for singlet cells and 31% purity for budding stages.[14] Beyond yeast, a range of designs have been engineered to sort differently-shaped microalgae[20,21] and spermatozoids,[22–25] to mention a few.

These last two applications (algae and spermatozoids) have another factor potentially impacting cell rotation (and hard to capture with model spherical beads): the presence of a flagellum. It has been shown previously that the flagella of spermatozoa, for instance, play a key role in focusing patterns,[26] preventing cells from rotating, which in turn affected shear-gradient forces, pushing only flagellated cells toward the device outer wall. However, this outward behaviour was still dependent on cell body size and shape, with biological heterogeneity leading to reduced focusing quality.

In this work, we investigate more closely the impact of cell body shape and flagella on focusing patterns in curved IM devices. More specifically, we modified (through chemical treatment and cell differentiation) the morphology of the naturally elongated, prolate-like kinetoplastid parasite *Leishmania mexicana* in order to vary its size, shape and/or flagellated status. High-throughput imaging flow cytometry was used to characterise cells' features, and single cell high-speed imaging was carried out in curved IM devices to analyse the effect of these features on cell focusing. We demonstrate that shape – but not the presence of flagella (for the studied cells) – plays a critical role in particle focusing, with parasites having different equilibrium positions depending on their aspect ratio or compared to size-matched beads. While higher Reynolds numbers typically led to more effective shape-based separation from beads, we found that parasites can be tightly focused to a unique focusing position, despite significant cell size and shape heterogeneity. These findings highlight the complex interplay between cells and fluid dynamics in curved systems, paving the way to a better understanding of IM devices for non-spherical cells.

Materials and methods

Cell preparation

Leishmania mexicana M379 Cas9 T7 promastigotes[27] were cultured according to[28] in medium 199 (Gibco™) supplemented with 10% foetal bovine serum (FBS; Gibco™), 26.2 mM sodium bicarbonate, 0.005% haemin, 40 mM 4-(2-hydroxyethyl)piperazine-1-ethanesulfonic acid pH 7.4, 32 μM hygromycin and 50 μM nourseothricin sulphate at 27 °C. Analysis was carried out on cells in their logarithmic stage of growth (1×10^6–7×10^6 cells per ml). Cells were deflagellated using a modification of the protocol outlined in ref. 29. Cells were fixed in 4% paraformaldehyde (PFA) in phosphate buffered saline (PBS) for 15 minutes at 4 °C and washed 3× in PBS, before being resuspended in 5 ml of a solution of 10 mM 1,4-piperazinediethanesulfonic acid (PIPES), 1 mM $CaCl_2$, 1 mM $MgCl_2$ and 0.32 M sucrose adjusted to pH 7.2. $CaCl_2$ was added to a final concentration of 0.075 M, and the sample was kept on ice. Flagella were removed from the cell bodies by drawing the resuspended cells through a 10 ml syringe fitted with a gel loading pipette tip 200 times. Sucrose gradient centrifugation was carried out as described in ref. 29 to isolate the deflagellated cell bodies from cells still possessing a flagellum, cell fragments and sheared flagella. The cell body fraction was washed with PBS prior to use in imaging flow cytometry or inertial microfluidic experiments. Axenic amastigotes were generated by culturing mid-log phase M379 Cas9 T7 cells in Schneider's *Drosophila* medium (Gibco™) pH 5.5, supplemented with 10% FBS at 32 °C for at least 72 hours. To synchronise cells in different cell cycle stages, mid-log phase parasites were incubated with either 5 mM hydroxyurea (Sigma; to arrest at G1/S phase) or 5 μM flavopiridol (Selleck Chemicals; to arrest in G2 phase) for 10 hours before being harvested and washed in PBS. Cells were then fixed with 4% PFA/PBS for 15 minutes at 4 °C and washed 3× in PBS prior to testing.

Cell characterisation using imaging flow cytometry

Morphological analysis of both live and fixed cells was carried out using imaging flow cytometry. Samples were resuspended in 60 μl PBS prior to acquisition on a Cytek® Amnis® ImageStream®X Mk II. ~30 000 events were acquired for each sample using INSPIRE™ software, collecting data from the brightfield channel using a 60× objective lens. The subsequent files were analysed using IDEAS® to extract morphological measurements of individual cells. The cell body mask and the gating strategy outlined in ref. 30 were used to remove images containing speed beads (added to the sample during acquisition for calibration purposes), debris, cell rosettes, two cells and out of focus cells. Area, aspect ratio (the minor axis of a fitted ellipsoid *vs.* the major axis), length and width measurements were calculated for the remaining population of cells and the data were exported from IDEAS® for further analysis in R. Data smoothing was carried out for the length and width measurements to account for the relatively low resolution of the images (length and width measurements are calculated in IDEAS® in increments of 0.33 µm and 0.66 µm, respectively). For this, a randomised number between −0.33 and 0.33 was added to each length measurement, and between −0.66 and 0.66 for width measurement.

Bead specifications

Various shapes and sizes of polystyrene beads were tested throughout this work. Spherical beads (3 and 5 µm in diameter) were sourced from Magsphere Inc. along with 2.6 × 3.2 µm^2, 2.5 × 4.0 µm^2, and 3.8 × 5.1 µm^2 pear-shaped beads and 2.8 × 4.0 µm^2, 4.5 × 6.3 µm^2, 5.1 × 7.7 µm^2 peanut-shaped beads. Spherical beads (4, 6, 8 and 10 µm in diameter) were sourced from Invitrogen.

Microfluidic setup

The microfluidic chips (Epigem) used in this work consisted of a 6-turn Archimedean spiral with an inlet and four outlets. Two sizes of chips were used with a channel height and width of either 30 × 170 µm^2 or 60 × 360 µm^2. Both bead and cell samples were prepared in PBS to a concentration of 5 × 10^5 particles per ml for IM analysis and injected into the smaller device at flow rates of 0.2–1.5 ml min^{-1} (Re = 33.3–250) or the larger device at 0.3–4.0 ml min^{-1} (Re = 23.8–317.5). A Nemesys high pressure pump (Cetoni) was used to pump the samples through 1/16″ polytetrafluoroethylene (PTFE) tubing with an internal diameter of 0.5 mm. Particle focusing behaviour was analysed using an AcCellerator cell analyser (Zellmechanik), which consisted of a high-speed camera and an inverted microscope. The chips were imaged using either a 20× or 10× objective for the smaller or larger device, respectively. The focusing position of the particles was acquired using the AcCellerator cell analyser's Shape-In (version 2.5.5.815) software to acquire images of each cell within the channel at 100 frames per second (fps). Analysis was carried out in Shape-Out 2 (version 2.13.6) to extract the position of the particles within the channel, which were subsequently analysed and plotted in R. The Reynolds numbers used were calculated according to ref. 31 using the equation: $\mathrm{Re} = pU_{\max}D_{\mathrm{h}}/u$, where p = fluid density (1000 kg m^{-3}), $U_{\max}$ = average fluid velocity, u = fluid viscosity (0.001 kg m^{-1} s^{-1}) and D_{h} = hydraulic diameter. D_{h} is calculated using the channel height (h) and width (w) measurements, given as $D_{\mathrm{h}} = 2hw/(h + w)$.

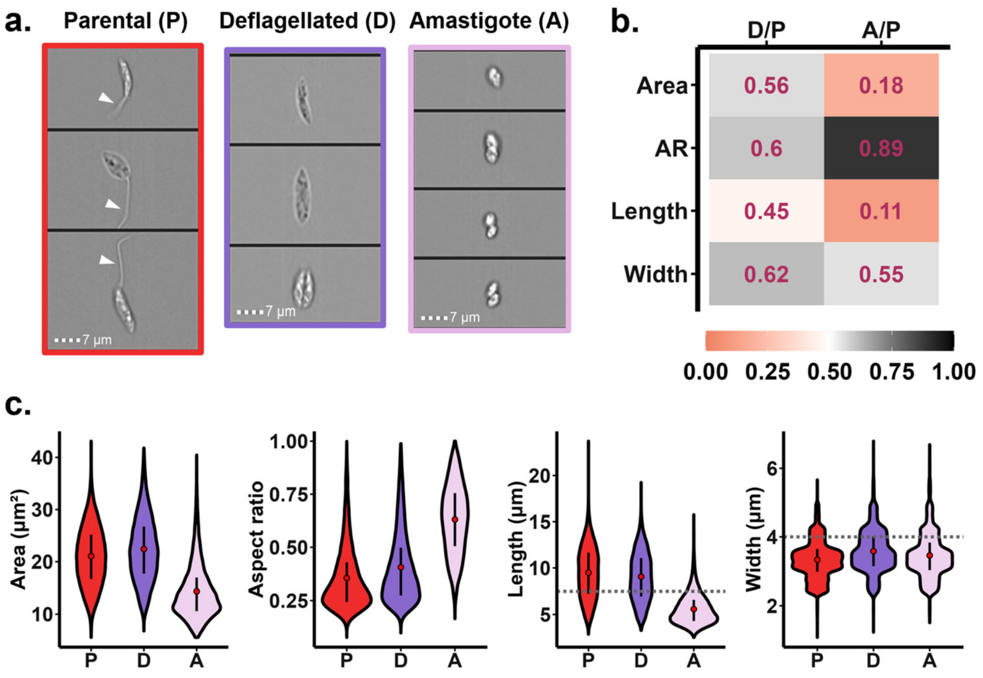

Fig. 1 Characterisation of the morphological phenotype of fixed parasites with and without flagella using imaging flow cytometry. (a) Example images of fixed parental (P), deflagellated (D) and amastigote (A) cells. The white arrowheads identify cell flagella. Scale bars: 7 µm. (b) Comparison of the area, aspect ratio (AR), length and width distributions between deflagellated and parental samples (D/P), and amastigote and parental cell population (A/P), as calculated from the area under the curve. A score close to 0.5 represents a distribution with a high similarity to the parental cell population, while a score closer to 0 or 1 denotes a high deviation in the distribution of measurements. A value <0.5 or >0.5 indicates that the morphological measurements are smaller or larger than the parental cells, respectively. (c) Violin plots depict the area, aspect ratio, length, and width distributions of the different cell populations. The red circles show the mean value, the black bars the 25th to 75th percentiles and the dotted grey lines indicate the thresholds applied to the length and width measurements (7.5 µm and 4.0 µm, respectively; $n \geq 12\,962$). See Table SI a† for raw data.

Results

Impact of flagella on focusing patterns

Promastigote *Leishmania mexicana* parasites were used as the biological model in this study for their elongated body shape and flagellated status. When cultured *in vitro*, these parasites typically form mixed populations of cells, which vary in size and shape according to their stage in the cell cycle (G1, S, G2, mitosis (M) and cytokinesis).[30,32] This untreated, mixed population of parasites is named hereafter the parental cell population. Two approaches were taken to investigate the impact of flagella on highly heterogeneous body shapes – chemical deflagellation and differentiation. Chemical deflagellation was carried out in line with previous work[29] while differentiation was used to generate axenic amastigotes. Amastigotes are the mammalian-infective stage of the parasite, which naturally possess only a vestigial flagellum presenting as a small bulbous tip that emerges from the cell body, yet the internal structures associated with this organelle are maintained.[33] Fig. 1a depicts examples of brightfield images collected with the imaging flow cytometer for the three conditions (parental, deflagellated and amastigotes), with the flagella clearly visible for the parental promastigotes. Analysis of thousands of cell images confirmed that chemically deflagellated cells had a similar range of morphologies to parental cells (Fig. 1c), with a maximum deviation of 0.12 from 0.5 when comparing the area under the curve (AUC; Fig. 1b). In contrast, as reported in the literature,[34] amastigotes were significantly shorter (average length of 5.5 µm, compared to 9.5 µm for parental promastigotes) and rounder (mean aspect ratio of 0.63, compared to 0.35 and 0.41 for parental and deflagellated parasites, respectively) with a width comparable to that of parental cells (average width of 3.5 µm, compared to 3.3 µm for parental). This is similarly demonstrated by the AUC values, in which area, aspect ratio and length demonstrate high deviations from 0.5.

While considerable variations in size and shape were observed within all cell populations (for example, the length of parental cells ranged from ∼3 to 15 µm, reflecting their cell cycle stage heterogeneity), the majority (∼60.7%, Fig. 2) of parental and deflagellated cells were long (>7.5 µm in length) and narrow (<4 µm in width), while amastigotes were predominantly (73.5%) short (≤7.5 µm in length) and narrow. These length and width thresholds were chosen to be relevant to the dimensions of the 30 × 170 µm^2 channel used: 7.5 µm corresponds to $\frac{1}{4}$ of the channel height (∼half of a Dean vortex, assuming two vortices) while a width of 4 µm provides a particle confinement ratio (λ) > 0.07 (the value above which particle focusing can be promoted).[31]

To characterise the focusing behaviour of these three cell populations, single cell high-speed imaging was performed near the outlet of a spiral IM channel. In such a design (Fig. 3a), spherical rigid particles with an equivalent diameter of 10 µm typically focused at the inner wall for the range of Reynolds numbers investigated in this work (up to Re = 250.0, Fig. 3b and c), and data are consequently presented as distances from the inner wall. While some enrichment was seen at the inner wall for the parental population at Reynolds numbers of 83.3 and 116.7 (Fig. 3d and e), both the inherently elongated parental and deflagellated parasites predominantly focused close to the outer wall for Reynolds number of 116.7 and above, which confirmed that in a curved channel, a particle's rotational diameter is not equivalent to the diameter of a spherical particle as has been previously reported.[14,31] Instead, this indicated an increased contribution of shape on focusing patterns. Furthermore, few differences were observed in the focusing behaviour between the parental and deflagellated parasites, indicating that the presence of a flagellum, for a conserved morphology, does not significantly alter focusing patterns for the tested conditions.

In contrast, amastigotes with a short, narrow and higher aspect ratio morphology (a morphology closer to that of spherical beads) focused tightly to the inner wall at lower Reynolds numbers (≤166), with >80% of cells focusing within a 17 µm band at Re = 83.3 (Fig. 3b). As the Reynolds number increased,

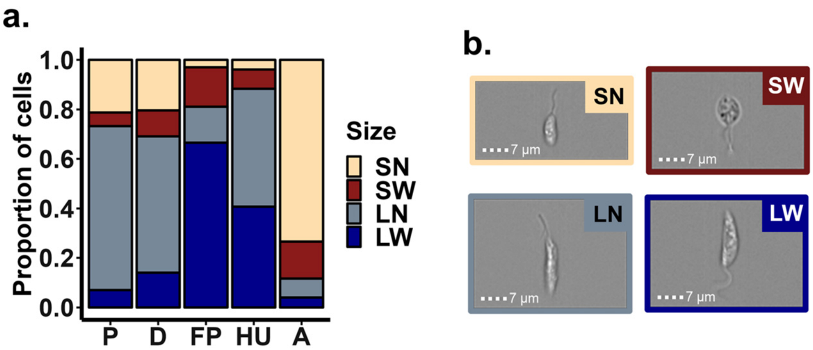

Fig. 2 Distributions of cell shape. Two thresholds were applied to provide a deeper characterisation of the cell morphologies present in the parental (P), deflagellated (D), flavopiridol- (FP) and hydroxyurea-treated (HU) cells, and amastigotes. These thresholds correspond to the cell length above or below 7.5 µm (which corresponds to one quarter of the channel height), and cell width above or below 4 µm (provides a λ > 0.07). (a) For each cell population, every cell was classified into a short (≤7.5 µm long) and narrow (<4 µm wide) (SN), short and wide (≥4 µm wide) (SW), long (>7.5 µm in length) and narrow (LN) or long and wide (LW) category (n > 12 962). (b) Examples of morphologies in each category, demonstrated with parental cells. Scale bars: 7 µm. See Table SI b† for raw data.

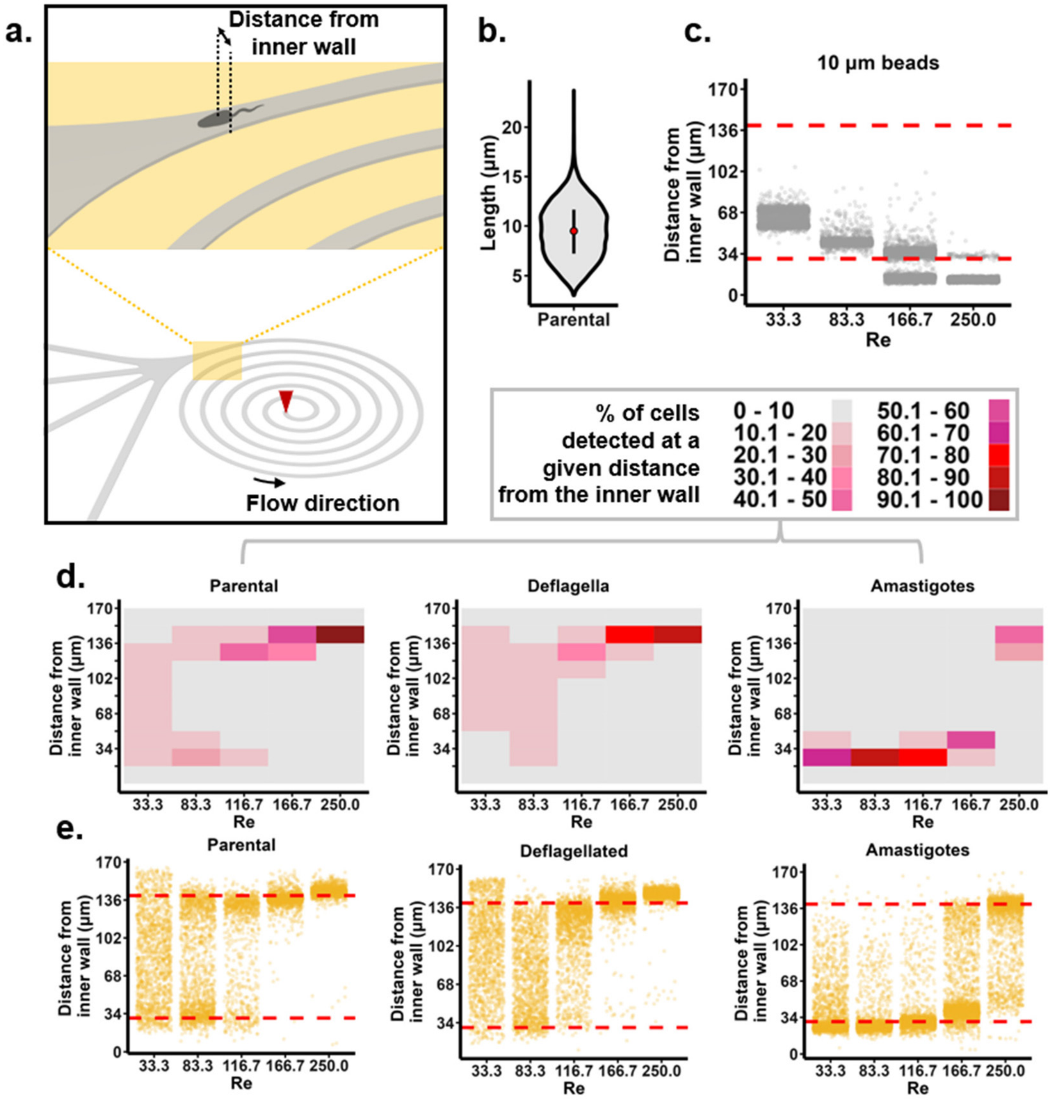

Fig. 3 Characterisation of the focusing behaviour of fixed parental, deflagellated and amastigote cells in a spiral inertial device. (a) Schematic of the inertial spiral channels used in this study (either with a cross section of 30 × 170 μm^2 or 60 × 360 μm^2), with a zoomed-in view near the outlet. The red arrow depicts the sample inlet and fixed parasites were imaged next to the opening for the outlet. Single cells were imaged using a high-speed camera and their location within the image was automatically extracted using Shape-In software. Their relative position within the channel was thus calculated as the distance from the inner wall (max distance = 170 μm or 360 μm). (b) The distribution of lengths of fixed *L. mexicana* cells, with a mean of 9.5 μm. The violin plot shows the mean as the red circle and the black bar the 25th–75th percentiles. (c) The focusing position of spherical 10 μm beads within a 30 × 170 μm^2 channel as analysed using a high-speed camera. Each individual dot corresponds to a single particle imaged in the channel. Red dashed reference lines indicate 30 μm from the inner and outer wall. See Tables SI a and c† for raw data. (d) Percentage of parasites ($n \geq 965$) focusing at a given distance from the inner wall of the 30 × 170 μm^2 device (channel width has been divided into 10 sections), with red zones highlighting a high focusing concentration with >70% of cells found within a tenth of the channel width. (e) Representation of focusing patterns with individual dots corresponding to a single parasite ($n \geq 965$) detected in the region of interest. The red dashed lines indicate a distance from the inner wall of 30 and 140 μm as a reference. Re denotes the Reynolds number. See Table SI d† for raw data.

the cells were seen to shift towards the outer wall. Interestingly, for the highest tested Reynolds number (Re = 250), ≥60% of cells from each population analysed (parental, deflagellated and amastigote) were concentrated within a 34 μm (119–153 μm from the inner wall) region close to the outer wall – irrespective of their significant morphological differences.

To further validate the effects of shape on sorting, live parental cells were sorted at Re = 116.7 into four outlets and the morphology of the cells in each outlet was analysed (Fig. 4a). From these data, the biggest change in the distribution of morphologies, when compared to the unsorted control, was seen at the inner wall for aspect ratio (AUC of 0.63; Fig. 4b). This corresponded to an enrichment of short and wide cells (*i.e.* a higher aspect ratio) at the inner wall (1.9× enrichment compared to the unsorted control; Fig. 4c), while short and narrow cells were evenly distributed between the outlets at the inner

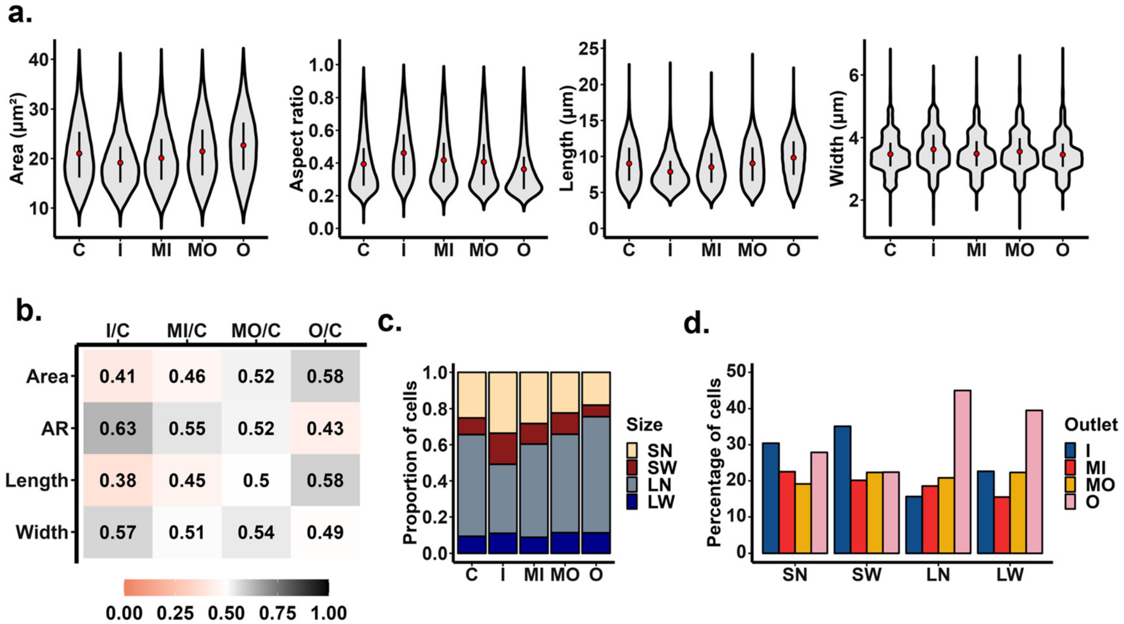

Fig. 4 Sorting of live *L. mexicana* enriches for short and wide cells. Live parental *L. mexicana* were sorted at Reynolds number Re = 116.7, and the sorted populations were collected at the four outlets of a spiral IM device with a channel cross section of 30 × 170 μm^2. Imaging flow cytometry analysis was carried out on an unsorted control (C) and the populations collected from the inner (I), middle inner (MI) middle outer (MO) and outer (O) outlets after sorting. (a) The area, aspect ratio, length, and width were plotted as a violin plot for each population, with the red circle showing the mean and the black bar the 25th–75th percentiles ($n \geq 18\,539$). (b) Comparison of the area, aspect ratio (AR), length and width distributions between the unsorted control population and the each of the different outlets, calculated from the area under the curve. A score close to 0.5 represents a minimum deviation from the unsorted control population, a value of <0.5 indicates values smaller than the control while a value >0.5 demonstrates a value larger than that of the control. (c) The distribution of sizes of cells sorted into each outlet ($n \geq 18\,539$). The cells from each sample were classified based on their size into short (S, ≤7.5 µm in length) or long (L, >7.5 µm in length) and narrow (N, <4 µm in width) or wide (W, ≥4 µm in width). (d) The percentage of cells of each size category sorted into each outlet ($n \geq 18\,539$). See Tables SI e and f† for raw data.

and outer wall (30.4% *vs.* 27.9%, respectively; Fig. 4d). Long and narrow cells on the other hand were predominantly found at the outlet closest to the outer wall (45.0%), with only 15.6% at the inner wall.

Impact of cell shape on focusing patterns

We then explored whether the shared focusing position at high Reynolds number observed in Fig. 3 for parental, deflagellated and amastigotes close to the outer wall was translatable to a wider range of cell shapes. Two additional cell populations were tested, with their characterisations presented in Fig. 5: flavopiridol-treated (FP) and hydroxyurea-treated (HU) cell populations. Parental parasites were chemically treated to arrest cells at specific stages (and consequently morphologies) of the cell cycle. Flavopiridol-treated cell populations – mostly arrested in G2 phase[30] – had a similar distribution of length to the untreated parental cells (mean length of 10.0 µm, compared to 9.5 µm for parental with an AUC of 0.54) but were generally wider (mean width of 4.9 µm, compared to 3.3 µm for parental and an AUC of 0.92). Hydroxyurea-treated cell populations on the other hand, reported to arrest other *Leishmania* spp.at G1/S,[35,36] had a highly similar distribution of aspect ratio sizes, with an AUC of 0.48 compared to the parental, but had an increase in the proportion of longer and wider cells (Fig. 2 and 5b).

Looking at the focusing position of parasites with these modified cell morphologies, different trends emerged (Fig. 6). To analyse cells with a higher rotational diameter but with a similar aspect ratio, hydroxyurea-treated cells were first compared to the parental population. At Re = 83.3 and 116.7, both populations concentrated at two concurrent focusing points, namely ~30 µm from the inner and outer wall (Fig. 6a, and S1†). Interestingly, a higher proportion of hydroxyurea-treated cells focused towards the inner wall at these same flow rates. This was unexpected as in Fig. 4 it was seen that longer parental cells predominantly focused to the outer wall. The increase in the proportion of long hydroxyurea-treated cells at the inner wall may be explained by differences in particle rotation: when comparing images taken with the high-speed camera (Fig. 6c–e), elongated cells that focused towards the inner wall predominantly adopted an orientation perpendicular to the channel walls, while cells focusing towards the outer wall seemed to align with the flow. It can also be observed that the cells aligned with the flow are all in focus, suggesting that they are at the same vertical position within the channel. The difference in particle rotation may be an effect of particle confinement, as parental cells had an average λ of 0.19, while HU-treated cells had a λ of 0.23. It is thus hypothesised that a low aspect ratio is required for particles to both align with the flow and focus to the outer wall, and above a certain confinement,

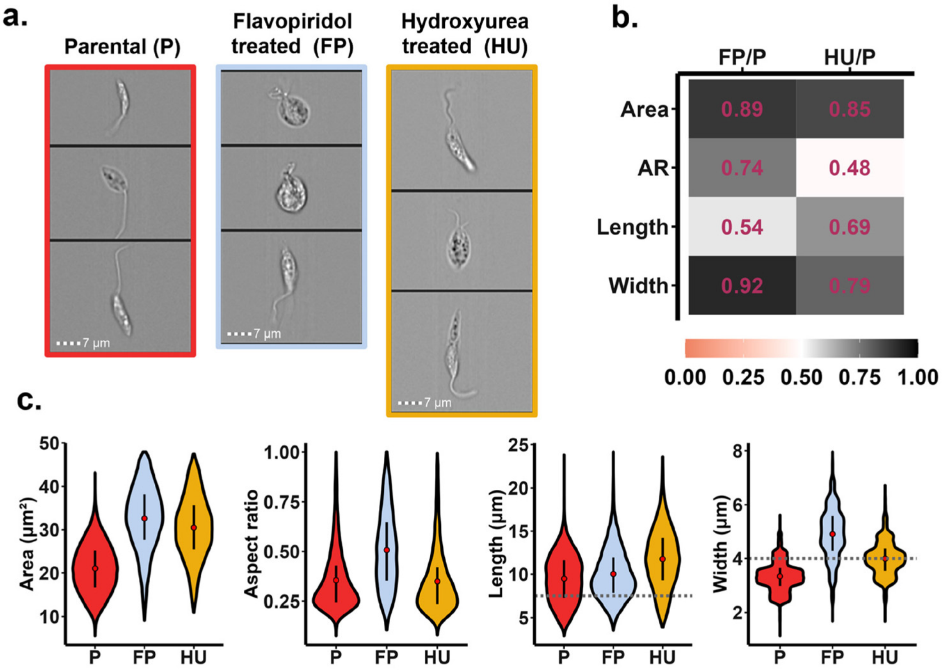

Fig. 5 Characterisation of the morphology of cell cycle-arrested *L. mexicana* using imaging flow cytometry. (a) Example images of fixed parental (P), flavopiridol-treated (FP) and hydroxyurea-treated (HU) cell populations. Scale bars: 7 µm. (b) Comparison of the area, aspect ratio (AR), length and width distributions between FP-treated and parental cells (FP/P), and HU-treated and parental (HU/P), calculated as the area under the curve. A score close to 0.5 represents a distribution with a high similarity to the parental cell population, while a score closer to 0 or 1 denotes a high deviation in the distribution of measurements. A value <0.5 or >0.5 indicates that the measurements are smaller or larger than the parental cells, respectively. (c) Violin plots depict the area, aspect ratio, length and width distributions of the different cell populations with the red circle showing the mean value and the black bars the 25th–75th percentiles ($n \geq 12\,962$). See Table SI a† for raw data.

particle rotation is modified such that particles maintain a horizontal alignment and focus to the inner wall. Elongated cells, therefore, may exhibit different focusing patterns, either at the inner wall or outer wall, depending on the Reynolds number, their aspect ratio, and their confinement within the channel.

In contrast, increasing the width but not the length of cells (thereby increasing the aspect ratio) seemed to result in the parasites being more dispersed throughout the channel, as seen for flavopiridol-treated cells at Re $\leq$ 116.7 (Fig. 6 and S1†). This contradicts the literature which has reported that the length and not the width of non-spherical beads has an effect on focusing,[14] further suggesting that aspect ratio is an important consideration for the focusing of non-spherical cells. Similarly to the other cell types tested, at high Reynolds numbers, both the hydroxyurea- and flavopiridol-treated cells occupied the same focusing position within ~30 µm from the outer wall.

In order to align our work with other studies, we compared these trends to both spherical and non-spherical rigid model particles.[19,20,37] We aimed to match these objects as closely as possible to some of the biological cells tested in this study, although the range of shapes available was manufacturer dependent.

The focusing behaviours of these beads are given in Fig. 7a, while a summary of the different morphologies tested is given in Fig. 7b. As shown in these figures, a variety of focusing behaviours were observed for the different particles tested. Initially, all sizes of spherical rigid objects tested (between 3 to 10 µm in diameter) focused tightly to the inner wall and none emulated the behaviours observed with parasites at the outer wall, as is consistent with the literature.[31] For non-spherical beads, an increase in the lateral migration away from the inner wall was observed compared to similarly sized spherical beads – this is dependent on both particle size and the Reynolds number. For example, larger non-spherical particles demonstrate a higher degree of lateral migration compared to their spherical counter parts, particularly at higher Reynolds numbers. As described in other studies, closely matched beads with different shapes (such as those highlighted by blue arrowheads in Fig. 7b) were also seen here to behave differently from each other,[15] with peanut-shaped beads (aspect ratio ~0.70) showing the furthest migration to the outer wall. Despite this, the focus was still significantly more spread than the one observed for parasites (with or without flagella). The same is seen when comparing similarly shaped cells and beads (*e.g.*, those highlighted by red and white arrowheads in Fig. 7b), with diverging focusing behaviours particularly at the highest Reynolds number tested; virtually no focusing within 30 µm of the outer wall was observed for any beads. These data confirm that shape plays a critical role in focusing patterns; however, as similarly shaped particles also differ in their focus-

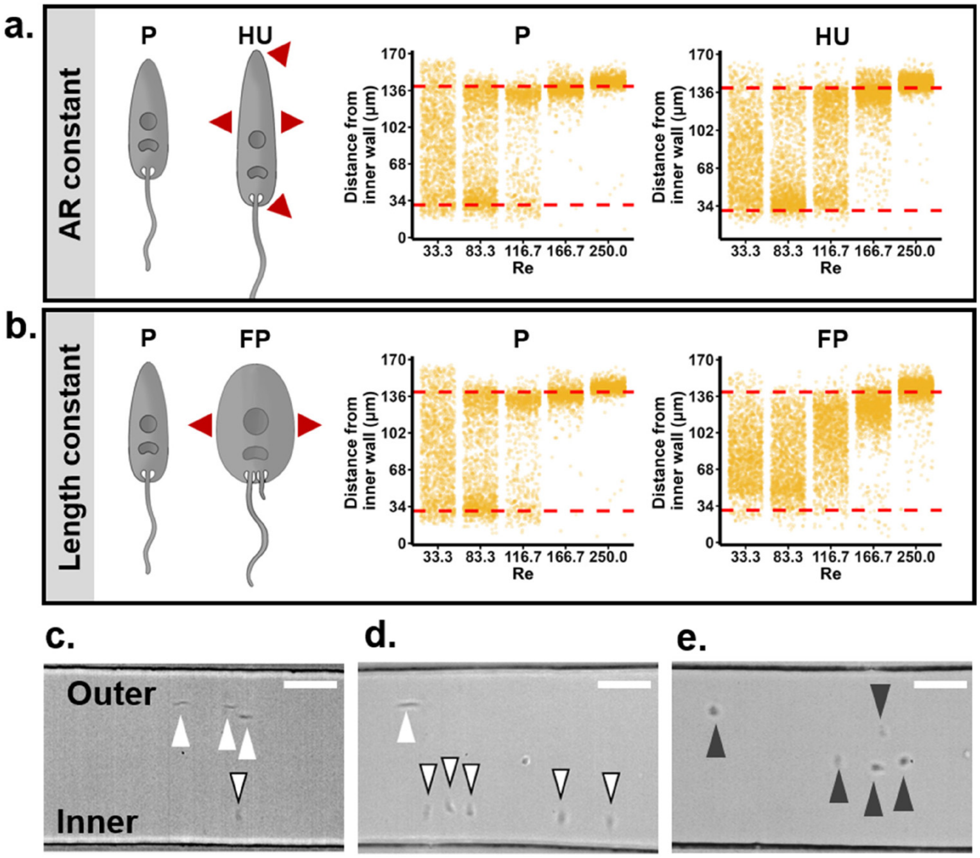

Fig. 6 Characterisation of the focusing behaviour of fixed parental, flavopiridol-treated (FP) and hydroxyurea-treated (HU) cell populations in a spiral inertial device. HU-treated cells (a) and FP-treated cells (b) are compared to parental cell populations. A graphical representation is given on the left of each panel, with the red arrows indicating the dimensions that were modified for both cell populations in comparison to the parental parasites. Single cells ($n \geq 965$) were imaged in the 30 × 170 μm^2 device using a high-speed camera and their position near the outlet were quantified as a distance from the inner wall (max distance = 170 µm). The red dashed reference lines indicate a distance of 30 µm from both the inner wall and outer walls. Re denotes the Reynolds number and the same graph for parental cells (P) is displayed for each panel (previously presented in Fig. 3e). See Table SI d† for raw data. High-speed images of *L. mexicana* parental cells (c), hydroxyurea-treated (d) and flavopiridol-treated (e) parasites focusing at a Reynolds number of 83.3 within the 30 × 170 μm^2 channel. Cells which are focused to the outer wall and aligned with the flow are identified with a solid white arrowhead, cells focusing towards the inner wall and oriented perpendicular to the channel walls are marked with bordered arrowheads, while cells with an undefined orientation and position are marked with black arrowheads. Scale bars: 50 µm.

ing positions, this is unlikely to be the sole reason for the parasites' focusing positions at the outer wall.

Alternative parameters were therefore tested to analyse their contribution to the parasites' focusing positions at the outer wall, specifically particle confinement and fluid dynamics (Fig. 8), both of which have previously been demonstrated to affect the focusing position of particles.[38,39]

In terms of particle confinement, previous results presented here demonstrated that differently sized and shaped parasites (amastigotes and parental cells with an average λ of 0.11 and 0.19, respectively) are capable of focusing at the outer wall at higher flow rates, with amastigotes also focusing to the inner wall at lower flow rates and requiring a higher Reynolds number to achieve the same degree of lateral migration. From Fig. 8a, it can be seen that with a lower confinement (λ of 0.09), parental cells have a focusing pattern more similar to that of amastigote cells (Fig. 3d and e), focusing tightly to the inner wall before moving to the outer wall with increasing Re. Around 50–70% of cells move to the outer wall at Re = 116.7 in the smaller channel, but >20% at Re = 119.0 in the larger channel. This confirms that confinement does play a role in the parasite's focusing position; however, as with amastigotes, a focusing position at the outer wall is still achieved, suggesting that the shape of the cells is still contributing to the final focusing position.

Finally, one can also suspect alterations to the fluid profile within microfluidic devices may be a cause for the parasites' unusual focusing position. For instance, simulations by Hafemann & Fröhlich (2023) demonstrated that prolate particles disturb the fluid velocity profile resulting in the formation of secondary vortices which led to a focusing position further from the inner wall.[17] Similarly, Nivedita demonstrated that at high Dean numbers, secondary Dean vortices formed which trapped both beads and cells at a stable focusing position at the outer wall.[39] Unfortunately, we were unable to replicate the experiments carried out by Nivedita to visualise any secondary vortices due to the thick PMMA devices used here. Instead, it was tested whether

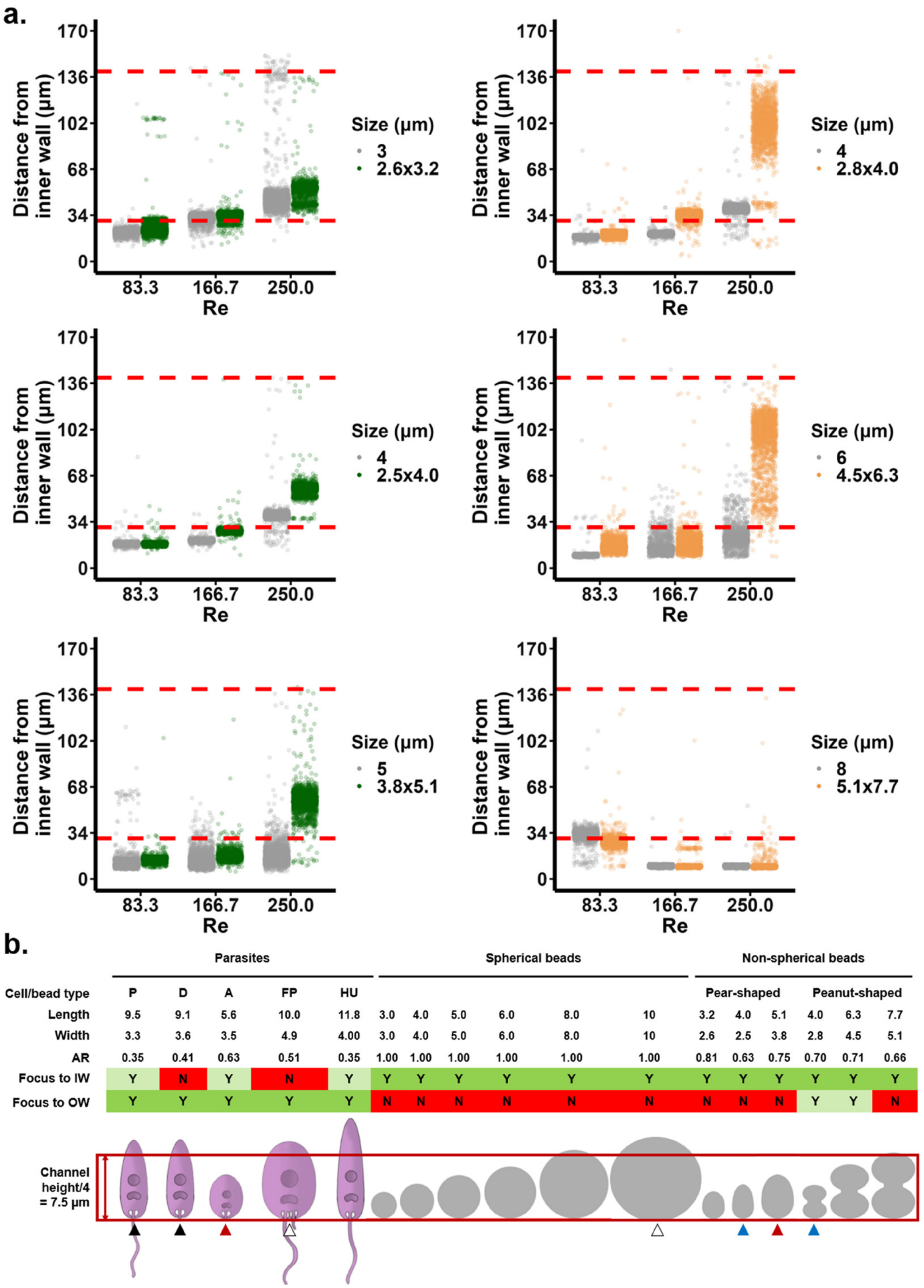

	Parasites					Spherical beads						Non-spherical beads					
Cell/bead type	P	D	A	FP	HU							Pear-shaped			Peanut-shaped		
Length	9.5	9.1	5.6	10.0	11.8	3.0	4.0	5.0	6.0	8.0	10	3.2	4.0	5.1	4.0	6.3	7.7
Width	3.3	3.6	3.5	4.9	4.00	3.0	4.0	5.0	6.0	8.0	10	2.6	2.5	3.8	2.8	4.5	5.1
AR	0.35	0.41	0.63	0.51	0.35	1.00	1.00	1.00	1.00	1.00	1.00	0.81	0.63	0.75	0.70	0.71	0.66
Focus to IW	Y	N	Y	N	Y	Y	Y	Y	Y	Y	Y	Y	Y	Y	Y	Y	Y
Focus to OW	Y	Y	Y	Y	Y	N	N	N	N	N	N	N	N	N	Y	Y	N

Fig. 7 Characterisation and summary of the focusing behaviour of the rigid particles and non-spherical cells. (a) Left graphs: focusing behaviour of pear-shaped beads of sizes 2.6 × 3.2 μm^2, 2.5 × 4.0 μm^2 and 3.8 × 5.1 μm^2 compared to that of spherical 3, 4 and 5 μm diameter beads, respectively. Right graphs: focusing behaviour of peanut-shaped beads of sizes 2.8 × 4.0 μm^2, 4.5 × 6.4 μm^2, and 5.1 × 7.7 μm^2 compared to spherical 4, 6 and 8 μm diameter beads, respectively. All sorting was carried out in the 30 × 170 μm^2 device, showing a single representative replicate for each sample. The spherical beads are shown in grey, the pear-shaped beads in green and the peanut-shaped beads in orange. Red dashed reference lines indicate positions 30 μm away from both the inner and outer walls ($n \geq 1500$). See Table SI c† for raw data. (b) Objects are characterised in this schematic by their average length (longest dimension, μm), width (shortest dimension, μm), and aspect ratio (AR). P, D, A, FP and HU denote parental, deflagellated, amastigote, flavopiridol- and hydroxyurea-treated cells, respectively. A green Y (Yes) or red N (No) indicates whether particle focusing was observed for at least one flow rate at 30 μm from the inner wall (IW) or 30 μm from the outer wall (OW). A light green Y denotes a focusing position within the outer half of the channel, but further than 30 μm from the outer wall. The morphological phenotype of particles was also compared to the channel quarter height (corresponding to half a Dean vortex). Arrows depict objects with the most similar morphologies: black for parental and deflagellated cells, red for amastigotes and pear-shaped beads, white for FP-treated and a spherical bead, and blue for pear- and peanut-shaped beads. See Table SI c† for raw data.

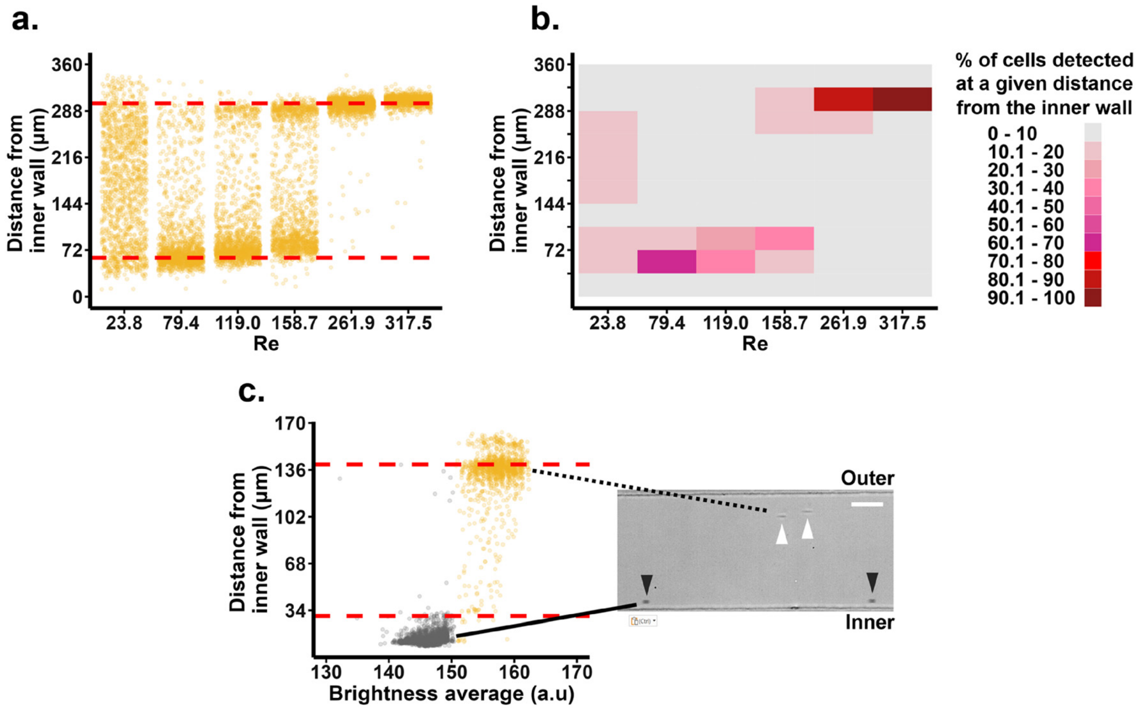

Fig. 8 Contribution of confinement, deformability and fluid dynamics to the focusing position of particles. Fixed *L. mexicana* were analysed for their focusing position in a channel with a cross section 60 × 360 μm^2. (a) The focusing position of individual cells ($n \geq 1500$) within the microfluidic channel as analysed by a high-speed camera. For the left-hand graph, the red dashed reference lines indicate a position 60 μm away from both the inner and outer wall. The data from the left-hand graph was quantified in the plot on the right-hand side to show the distribution of cells along the channel width. For each flow rate, the channel width was divided into 10 sections; each section corresponds to a distance of 36 μm. Each section was colour-coded (on a scale of 1–10) according to the percentage of cells falling within that section. Each colour bracket accounts for a 10% range. See Table SI h† for raw data. (c) A suspension of fixed *L. mexicana* parental cells and beads with a diameter of 5 μm was prepared and the focusing positions of the particles was analysed at a Reynolds number of 166.7 in the 30 × 170 μm^2 channel. The position of each particle in the channel was plotted against its average brightness (left), and reference lines 30 μm from the inner and outer wall are shown with dashed red lines (n = 5103). Objects with a brightness ≤150 arbitrary units (a.u.) were identified as beads (grey), while *Leishmania* cells had a brightness >150 a.u. (gold). An image containing both parental cells (white arrowheads) and 5 μm beads (black arrowheads) is given on the right, with the dotted black line identifying the population of parental cells focusing to the outer wall of the channel and the solid black line indicating 5 μm beads focusing to the inner wall. Scale bar: 50 μm. See Table SI i† for raw data.

the presence of the parasites modified the fluid velocity profile and thus affected the focusing position of beads. As can be seen from Fig. 8c, a mixture of parental parasites and 5 μm beads produced two distinct populations; particles with a lower average brightness (<150 a.u.) corresponded to 5 μm beads, and these focused to the inner wall. In contrast, the parental cells with a higher average brightness (>150 a.u.) remained at a focusing position at the outer wall. These positions are highly comparable to those obtained when these particles were analysed separately (Fig. 6a and 7, respectively). While this does not rule out the possibility of secondary vortices being formed, it further highlights that the morphology of the cells, as opposed to altered fluidic dynamics, is responsible for the parasites' migration to the outer wall.

Discussion

Although size and shape have both been exploited as sorting parameters in IM devices, one of the key challenges to better interpret results is the intrinsic variability in morphologies encountered in most biological systems. Without high-throughput characterisation of the morphological phenotype for a given cell population, conclusions on inertial focusing behaviours can be skewed or biased. Here we used high-speed imaging to not only characterise single cell behaviours in IM devices, but also to quantify morphological variations with high accuracy.

We first demonstrated that elongated prolate-like *L. mexicana* displayed a focusing position towards the outer wall at Reynolds numbers as low as 83.3. While focusing positions at the outer wall have been demonstrated before, it has never been reported as a result of particle shape alone, as seen in this work.[5,23,39] Deformability has been linked to a focusing position at the outer wall in other works;[5,9] here however, rigid, fixed *L. mexicana* parasites exhibited the same behaviour. It is possible that the migration of both elongated cells and deformable particles towards the outer wall at high flow rates occurs under the same mechanism, with deformable particles taking a more elongated morphology at high shear rate.[16] Furthermore, instead of rotating with the flow, these particles have been described to tank tread, with the particles thus maintaining a consistent deformed shape and behaving similarly to non-rotating elongated parasites.

Beyond deformability, focusing at the outer wall has also been attributed in the literature to the presence of flagella. Flagellated human spermatozoids (with a cell body ~4 μm in length and a flagella length of ~45 μm (ref. 40)) were observed to shift towards the outer wall, while deformable red blood cells or deflagellated spermatozoids remained at the inner wall.[23] It was consequently concluded that the presence of flagella prevented cell rotation and induced lateral migration. In a later study by Naderi *et al.*, particle tracking simulations demonstrated that the lack of rotation for flagellated sperm affected the shear-gradient force, resulting in a vertical lift.[25] This vertical lift caused the cells to be dragged by the Dean flow to the outer wall where they found an equilibrium position. Here, a similar theory around rotation is expected to account for the migration of the parasites to the outer wall; however, the phenomenon is driven by the parasites' elongated body shape as opposed to the flagella. Indeed, we observed that cells focusing at the outer wall align with the flow with seemingly no rotation. Additionally, Zettner and Yoda demonstrated that elongated particles ceased rotating and adopted a stable orientation above a critical Reynolds number.[13] They also demonstrated that an increase in confinement reduced the critical Reynolds number to cease particle rotation. Hur similarly demonstrated that non-rotating particles shift further away from the inner wall,[10,16] aligning with our findings.

Inertial focusing traditionally aims to sort different populations of cells. While we demonstrated a potential for sorting based on shape (achieving a 1.9× enrichment of short and wide cells in an unoptimised device), an additional result from our study is in the ability to tightly focus cells with highly heterogenous morphologies at a single equilibrium position at high Reynolds number. All the *L. mexicana* populations tested in this work – irrespective of their flagellated status, size, shape or chemical treatment – were observed to focus at the same equilibrium position ~30 μm away from the outer wall (distance equivalent to the channel height) at a high Reynolds number (~250.0). These findings were replicated in a larger $60 \times 360\ \mu m^2$ channel, with cells focusing ~60 μm away from the outer wall. Even rounder amastigotes shifted to this position, as opposed to size- and shape-matched polystyrene beads (for an equivalent range of Reynolds numbers). Such an ability to concentrate highly heterogenous populations of elongated cells is a novel observation, and has potential benefits in a wide range of applications, *e.g.* the dewatering of algae (*e.g.* for animal feed, carbon fixing and biofuel),[41] the removal of pathogens from drinking water for sanitation and quality control,[42,43] and the concentration of parasites for diagnostic purposes.[44,45] However, this diverges from Naderi *et al.*, who reported that variations in the shape and size of the sperm bodies caused imprecise focusing and is a phenomenon currently under further investigation.[25]

To conclude, the field of microfluidics and IM has been significantly enhanced by (imaging) cytometry[46–49] and this should be used, when possible, in tandem with IM characterisation to provide the most accurate representation of cell focusing patterns. We demonstrate that the relationship between particle shape, rotation and equilibrium position within IF devices is more complex than previously assumed, highlighting the need for further studies into the rotational behaviours of non-spherical particles in curved channels.

Author contributions

JH was responsible for conceptualisation, methodology, investigation, formal analysis, writing – original draft, and writing – review & editing. NH and SO contributed to conceptualisation and investigation, as well as writing – review & editing. TH contributed to conceptualisation and writing – review & editing. MJ contributed to conceptualisation, formal analysis, in addition to writing – original draft and writing – review & editing.

Conflicts of interest

There are no conflicts to declare.

Data availability

The data supporting this article have been included as part of the ESI and are contained within the file named "Table SI".† Reference to the data has been included within the article.

Acknowledgements

JH and NH would like to thank the Engineering and Physical Sciences Research Council (EPSRC) for their scholarships (EP/R513222/1 and EP/W524670/1). This project was supported by the Royal Academy of Engineering under the Research Fellowship programme (RF\201718\1741). MJ would like to thank the Royal Society for their support (RGS\R1\191188). SO is funded by a Cunningham Trust (**https://www.cunningham-trust.org.uk**) PhD studentship grant (PhD-CT-19-14) awarded to TH.

References

1 D. Di Carlo, Inertial microfluidics, *Lab Chip*, 2009, **9**(21), 3038–3046, DOI: **10.1039/B912547G**.

2 G.-Y. Kim, J.-I. Han and J.-K. Park, Inertial Microfluidics-Based Cell Sorting, *BioChip J.*, 2018, **12**(4), 257–267, DOI: **10.1007/s13206-018-2401-2**.

3 Q. Zhao, D. Yuan, J. Zhang and W. Li, A Review of Secondary Flow in Inertial Microfluidics, *Micromachines*, 2020, **11**(5), 461, DOI: **10.3390/mi11050461**.

4 D. Di Carlo, D. Irimia, R. G. Tompkins and M. Toner, Continuous inertial focusing, ordering, and separation of particles in microchannels, *Proc. Natl. Acad. Sci. U. S. A.*, 2007, **104**(48), 18892–18897, DOI: 10.1073/pnas.0704958104.

5 E. Guzniczak, O. Otto, G. Whyte, N. Willoughby, M. Jimenez and H. Bridle, Deformability-induced lift force in spiral microchannels for cell separation, *Lab Chip*, 2020, **20**(3), 614–625.

6 S. Ebrahimi and P. Bagchi, Inertial and non-inertial focusing of a deformable capsule in a curved microchannel, *J. Fluid Mech.*, 2021, **929**, A30, DOI: 10.1017/jfm.2021.868.

7 S. C. Hur, N. K. Henderson-MacLennan, E. R. B. McCabe and D. Di Carlo, Deformability-based cell classification and enrichment using inertial microfluidics, *Lab Chip*, 2011, **11**(5), 912–920, DOI: 10.1039/C0LC00595A.

8 H. W. Hou, *et al.*, Deformability based cell margination—A simple microfluidic design for malaria-infected erythrocyte separation, *Lab Chip*, 2010, **10**(19), 2605–2613, DOI: 10.1039/C003873C.

9 E. Guzniczak, *et al.*, Purifying stem cell-derived red blood cells: a high-throughput label-free downstream processing strategy based on microfluidic spiral inertial separation and membrane filtration, *Biotechnol. Bioeng.*, 2020, **117**(7), 2032–2045, DOI: 10.1002/bit.27319.

10 S. C. Hur, S.-E. Choi, S. Kwon and D. D. Carlo, Inertial focusing of non-spherical microparticles, *Appl. Phys. Lett.*, 2011, **99**(4), 044101, DOI: 10.1063/1.3608115.

11 T. Tohme, P. Magaud and L. Baldas, Transport of Non-Spherical Particles in Square Microchannel Flows: A Review, *Micromachines*, 2021, **12**(3), 277, DOI: 10.3390/mi12030277.

12 J. Einarsson, F. Candelier, F. Lundell, J. R. Angilella and B. Mehlig, Effect of weak fluid inertia upon Jeffery orbits, *Phys. Rev. E*, 2015, **91**(4), 041002, DOI: 10.1103/PhysRevE.91.041002.

13 C. M. Zettner and M. Yoda, Moderate-aspect-ratio elliptical cylinders in simple shear with inertia, *J. Fluid Mech.*, 2001, **442**, 241–266, DOI: 10.1017/S0022112001005006.

14 M. Masaeli, *et al.*, Continuous Inertial Focusing and Separation of Particles by Shape, *Phys. Rev. X*, 2012, **2**(3), 031017, DOI: 10.1103/PhysRevX.2.031017.

15 T. Roth, L. Sprenger, S. Odenbach and U. O. Häfeli, Continuous form-dependent focusing of non-spherical microparticles in a highly diluted suspension with the help of microfluidic spirals, *Phys. Fluids*, 2018, **30**(4), 045102, DOI: 10.1063/1.5019843.

16 H. Amini, W. Lee and D. Di Carlo, Inertial microfluidic physics, *Lab Chip*, 2014, **14**(15), 2739–2761, DOI: 10.1039/C4LC00128A.

17 T. Hafemann and J. Fröhlich, Simulation of non-spherical particles in curved microfluidic channels, *Phys. Fluids*, 2023, **35**(3), 033328, DOI: 10.1063/5.0139105.

18 S. Sofela, *et al.*, High-throughput sorting of eggs for synchronization of C. elegans in a microfluidic spiral chip, *Lab Chip*, 2018, **18**(4), 679–687, DOI: 10.1039/C7LC00998D.

19 E. Keinan, *et al.*, High-Reynolds Microfluidic Sorting of Large Yeast Populations, *Sci. Rep.*, 2018, **8**(1), 13739, DOI: 10.1038/s41598-018-31726-6.

20 A. Schaap, J. Dumon and J. D. Toonder, Sorting algal cells by morphology in spiral microchannels using inertial microfluidics, *Microfluid. Nanofluid.*, 2016, **20**(9), 125, DOI: 10.1007/s10404-016-1787-1.

21 M. Li, H. E. Muñoz, K. Goda and D. Di Carlo, Shape-based separation of microalga Euglena gracilis using inertial microfluidics, *Sci. Rep.*, 2017, **7**(1), 10802, DOI: 10.1038/s41598-017-10452-5.

22 S. Nepal, H. Feng and B. K. Gale, Optimization of a microfluidic spiral channel used to separate sperm from blood cells, *Biomicrofluidics*, 2020, **14**(6), 064103, DOI: 10.1063/5.0029508.

23 H. Feng, *et al.*, High efficiency rare sperm separation from biopsy samples in an inertial focusing device, *Analyst*, 2021, **146**(10), 3368–3377, DOI: 10.1039/D1AN00480H.

24 H. Jeon, C. Cremers, D. Le, J. Abell and J. Han, Multi-dimensional-double-spiral (MDDS) inertial microfluidic platform for sperm isolation directly from the raw semen sample, *Sci. Rep.*, 2022, **12**(1), 4212, DOI: 10.1038/s41598-022-08042-1.

25 M. M. Naderi, H. Gao, J. Zhou, I. Papautsky and Z. Peng, Deciphering the unique inertial focusing behavior of sperm cells, *Lab Chip*, 2025, **25**(12), 2874–2886, DOI: 10.1039/D5LC00047E.

26 A. Ryabov, *et al.*, Shape matters: the relationship between cell geometry and diversity in phytoplankton, *Ecol. Lett.*, 2021, **24**(4), 847–861, DOI: 10.1111/ele.13680.

27 T. Beneke, R. Madden, L. Makin, J. Valli, J. Sunter and E. Gluenz, A CRISPR Cas9 high-throughput genome editing toolkit for kinetoplastids, *R. Soc. Open Sci.*, 2017, **4**(5), 170095, DOI: 10.1098/rsos.170095.

28 T. Beneke and E. Gluenz, LeishGEdit: A Method for Rapid Gene Knockout and Tagging Using CRISPR-Cas9, in *Leishmania: Methods and Protocols*, ed. J. Clos, Springer New York, New York, NY, 2019, pp. 189–210.

29 T. Beneke, F. Demay, R. J. Wheeler and E. Gluenz, Isolation of Leishmania Promastigote Flagella, in *Trypanosomatids: Methods and Protocols*, ed. P. A. M. Michels, M. L. Ginger and D. Zilberstein, Springer US, New York, NY, 2020, pp. 485–495.

30 J. Howell, S. Omwenga, M. Jimenez and T. C. Hammarton, Analysis of the Leishmania mexicana promastigote cell cycle using imaging flow cytometry provides new insights into cell cycle flexibility and events of short duration, *PLoS One*, 2024, **19**(10), e0311367, DOI: 10.1371/journal.pone.0311367.

31 J. M. Martel and M. Toner, Particle Focusing in Curved Microfluidic Channels, *Sci. Rep.*, 2013, **3**(1), 3340, DOI: 10.1038/srep03340.

32 R. J. Wheeler, E. Gluenz and K. Gull, The cell cycle of Leishmania: morphogenetic events and their implications for parasite biology, *Mol. Microbiol.*, 2011, **79**(3), 647–662, DOI: 10.1111/j.1365-2958.2010.07479.x.

33 J. Sunter and K. Gull, Shape, form, function and Leishmania pathogenicity: from textbook descriptions to biological understanding, (in eng), *Open Biol.*, 2017, **7**(9), 170165, DOI: **10.1098/rsob.170165**.

34 F. Dagger, C. Bengio, A. Martinez and C. Ayesta, Leishmania mexicana differentiation involves a selective plasma membrane autophagic-like process, (in eng), *Cell Stress Chaperones*, 2018, **23**(4), 783–789, DOI: **10.1007/s12192-017-0864-z**.

35 B. C. D. de Oliveira, *et al.*, Synchronization of Leishmania amazonensis Cell Cycle Using Hydroxyurea, in *Cell-Cycle Synchronization: Methods and Protocols*, ed. Z. Wang, Springer US, New York, NY, 2022, pp. 127–135.

36 L. Simpson and P. Braly, Synchronization of Leishmania tarentolae by Hydroxyurea, *J. Protozool.*, 1970, **17**(4), 511–517, DOI: **10.1111/j.1550-7408.1970.tb04719.x**.

37 L. Ding, S. Razavi Bazaz, T. Hall, G. Vesey and M. Ebrahimi Warkiani, Giardia purification from fecal samples using rigid spiral inertial microfluidics, *Biomicrofluidics*, 2022, **16**(1), 014105, DOI: **10.1063/5.0069406**.

38 W. E. Uspal, H. Burak Eral and P. S. Doyle, Engineering particle trajectories in microfluidic flows using particle shape, *Nat. Commun.*, 2013, **4**(1), 2666, DOI: **10.1038/ncomms3666**.

39 N. Nivedita, P. Ligrani and I. Papautsky, Dean Flow Dynamics in Low-Aspect Ratio Spiral Microchannels, *Sci. Rep.*, 2017, **7**(1), 44072, DOI: **10.1038/srep44072**.

40 P. Sunanda, B. Panda, C. Dash, R. N. Padhy and P. Routray, An illustration of human sperm morphology and their functional ability among different group of subfertile males, *Andrology*, 2018, **6**(5), 680–689, DOI: **10.1111/andr.12500**.

41 J. Jeevanandam and M. K. Danquah, Chapter 9 – Dewatering and drying of algal cultures, in *Handbook of Microalgae-Based Processes and Products*, ed. E. Jacob-Lopes, M. M. Maroneze, M. I. Queiroz and L. Q. Zepka, Academic Press, 2020, pp. 207–224.

42 C. Hill, N. Willoughby and H. Bridle, Efficient high-concentration dewatering of Chlorella vulgaris utilising spiral inertial microfluidics, *Bioresour. Technol. Rep.*, 2022, **18**, 101014, DOI: **10.1016/j.biteb.2022.101014**.

43 W. Quintero-Betancourt, E. R. Peele and J. B. Rose, Cryptosporidium parvum and Cyclospora cayetanensis: a review of laboratory methods for detection of these waterborne parasites, *J. Microbiol. Methods*, 2002, **49**(3), 209–224, DOI: **10.1016/S0167-7012(02)00007-6**.

44 B. B. Fuchs, S. Eatemadpour, J. M. Martel-Foley, S. Stott, M. Toner and E. Mylonakis, Rapid Isolation and Concentration of Pathogenic Fungi Using Inertial Focusing on a Chip-Based Platform, (in English), *Front. Cell. Infect. Microbiol.*, 2019, **9**(27), DOI: **10.3389/fcimb.2019.00027**Original Research.

45 S. Momčilović, C. Cantacessi, V. Arsić-Arsenijević, D. Otranto and S. Tasić-Otašević, Rapid diagnosis of parasitic diseases: current scenario and future needs, *Clin. Microbiol. Infect.*, 2019, **25**(3), 290–309, DOI: **10.1016/j.cmi.2018.04.028**.

46 K. Lee, S.-E. Kim, S. Nam, J. Doh and W. K. Chung, Upgraded User-Friendly Image-Activated Microfluidic Cell Sorter Using an Optimized and Fast Deep Learning Algorithm, *Micromachines*, 2022, **13**(12), 2105, DOI: **10.3390/mi13122105**.

47 B. Dong, *et al.*, Real-time Functional Analysis of Inertial Microfluidic Devices via Spectral Domain Optical Coherence Tomography, *Sci. Rep.*, 2016, **6**(1), 33250, DOI: **10.1038/srep33250**.

48 Z. Wang, V. Bianco, P. L. Maffettone and P. Ferraro, Holographic flow scanning cytometry overcomes depth of focus limits and smartly adapts to microfluidic speed, *Lab Chip*, 2023, **23**(9), 2316–2326, DOI: **10.1039/D3LC00063J**.

49 G. Holzner, *et al.*, High-throughput multiparametric imaging flow cytometry: toward diffraction-limited sub-cellular detection and monitoring of sub-cellular processes, *Cell Rep.*, 2021, **34**(10), 108824, DOI: **10.1016/j.celrep.2021.108824**.